Ocean and Coastal Research

ORIGINAL ARTICLE

http://doi.org/10.1590/2675-2824073.24002
ISSN 2675-2824

Observations of the surface current field in morphologically complex environments using drones

Flavia Macedo[1], Carlos Augusto Schettini[1]*

[1] Universidade Federal de Rio Grande – Instituto de Oceanografia (Av. Itália km 8 -Campus Carreiros – 96203-900 – RS – Brazil)

* Corresponding author: guto.schettini@gmail.com

ABSTRACT

This study aims to analyze the use of drones to measure surface currents and make it accessible via package of routines generated using free software. Validation was performed in a complex environment comparing the results with currents measured by acoustic Doppler current profiler (ADCP) and dye tracers. Then, we assessed the performance of the method at various altitudes and image resolutions. We found equivalent values obtained by the drone with dye tracers and ADCP, confirming the efficiency of the technique. However, best agreement with the dye tracer, as it provide velocity near the surface, which is more compatible with the data generated by the drone. On the other hand, ADCPs generate measurements around 1 m below the surface due to acoustic signal interference near the surface and the level of the transducers. The use of drones showed promise, agreeing with direct observations, and low sensitivity for video recordings at lower resolutions, thus reducing processing time. The implementation of the technique in Python enables its use on free software. Based on the comparisons, we highlight the need for future studies to test the efficiency of the drone method at different altitudes and camera inclination angles, which would enable larger data collection areas.

Keywords: Hydrodynamics, Remote sensing, Python

INTRODUCTION

The advection of water, or currents, in coastal environments results from the action of pressure gradient forces generated by water level oscillations (tides or river inflow), horizontal density gradients, and wind shear stress at the surface interacting with the shores and the seabed (Mooers et al., 1976). Understanding the behavior of these currents is essential for comprehending the functioning of environments, as they are responsible for the transport and dispersion of dissolved and particulate materials in the water (Rodriguez et al., 2019). The interaction with soft boundaries leads to modifications, eroding or depositing sediments, and altering geomorphology (van Rijn, 1998).

Water bodies in the coastal zone can be semi-closed, such as estuaries, bays, fjords, and coastal lagoons (Valle-Levinson, 2022), as well as include the adjacent continental shelf (Bowden, 1883; Lentz, 2022). These are highly dynamic environments where changes in current patterns vary over broad scales of time and space. Situated in an area of intense socio-economic activity with the presence of urban centers, industries, and ports, the waters of these environments are subject to various human activities, including fishing, recreation, cargo transportation, as well as extraction and transportation related to the oil and gas industry

Submitted: 04-Jan-2024
Approved: 27-Dec-2024

Associate Editor: Piero Mazzini

(Halpern et al., 2008). Associated with these activities are environmental impacts that can be significant, especially near port areas due to the higher flow of vessels (Marone et al., 2020).

Conceptually, the study of currents is approached by two distinct and complementary methods: Eulerian and Lagrangian. Both are applied in coastal hydrodynamic studies, each presenting advantages and disadvantages. The Eulerian method involves measuring currents from a fixed position, resulting in time series for a specific coordinate and depth. Currently, the most used equipment for this purpose is the Acoustic Doppler Current Profiler (ADCP) (e.g., Fong and Monismith, 2004). ADCPs can be used in various ways, such as being installed on the seafloor aiming upward, on vessels aiming downward, or attached on piers aiming sideways. In the case of vessel mounted, the instrument can track the seafloor and measure absolute velocities from the moving vessel, allowing a spatial/vertical observation of the flow s. Lagrangian methods involve tracking a portion of the fluid, varying coordinates over time. An example of this methodology is the use of drifters, which are essentially buoys with GPS receivers.

The use of drifters or ADCPs requires a support vessel, which is often limiting due to associated logistics (costs and operational considerations), and there are alternative methods to measure currents using remote sensing. An alternative for obtaining the surface current field is radar technology. Radars can be installed on land and capture a wide area simultaneously and for long periods of time. High frequency radars (HF) are well established for monitoring shelf areas, with X-band radars being able to provide high resolution results in rivers and coastal areas (Chapman et al., 1997; Plant et al., 2009; Novi et al., 2020). However, the use of radars remains relatively restricted due to high costs and complex technology for data acquisition, as well as the time required for implementation.

Particle image velocimetry (PIV) is another option to measure currents in coastal environments. PIV refers to a class of methods used in experimental fluid mechanics to determine particles displacement in a moving fluid (Adrian and Westerweel, 2011). The concept is rather simpler than the use of radars: two snapshots taken by a fixed camera can provide the change of a reference point (particle displacement) over a time interval, which enables the estimation of particle velocity and direction. The camera can be in a fixed frame system (Chickadel et al., 2003; Holman and Stanley, 2007; Palmsten et al., 2015) or in a quadcopter drone hovering completely still in the air (Stresser et al., 2017; Fairley et al., 2022, 2024; Koutalakis and Zaimes, 2022).

The PIV technique for obtaining surface currents using drones involves tracking the displacement of particles, which is conceptually a Lagrangian approach. The particles can be naturally occurring markers, such as floating debris or foam, or specifically introduced ones like buoys or dye tracers. Studies by Chickadel et al. (2011) have successfully applied PIV techniques to measure surface currents in rivers using infrared imagery, further illustrating the flexibility of this approach. Additionally, Palmsten et al. (2015), have explored PIV in similar aquatic environments, providing important contributions to its application for monitoring surface flows.

Recently, Stresser et al. (2017) introduced a novel approach to obtain surface currents based on video recorded by quadcopter drones via wave dispersion relation, in which wave parameters are extracted from the variability in pixel intensity of images (Stresser et al., 2017). This technique presents a significant advantage over the PIV method since it does not require floating targets and provides the surface current field for the imaged area. The use of solely quadcopters drones for generating current fields, with no need for drifters or dye tracers, holds the advantage of ease and speed, contributing primarily to diagnostics that require quick decision-making for impact mitigation, in addition to being a cost-effective method. As it is relatively new, its applicability is being tested across various flow conditions, such as in rivers (Stresser et al., 2017), tidal channels (Fairley et al., 2022, 2024), and wind driven flows (Macedo et al., 2023). This study aimed to evaluate this method in a complex geometry environment, with variable depth and width, comparing the results with ADCP

records and dye tracer release. We also assessed the impact of drone altitude and video resolution, in addition to providing a free data processing code written in Python.

METHODS

Coding the Python Package

The Matlab code (Mathworks Inc) for obtaining currents from drone-recorded videos is available on GitHub (Carrasco, 2019). The first part of this study involved implementing the code in Python, motivated by the use of the technique with open-source software. The process of code translation and performance testing was primarily performed on a laptop with an Intel(R) Core (TM) i3-6006U CPU 2.00 GHz, 12 GB RAM, 64-bit operating system, x64-based processor, and Windows 10. Python 3.10 (https://www.python.org/) was used, working with the Jupyter-Lab IDE (https://jupyter.org/) and the MatLab R2020a version (https://www.mathworks.com/).

The packages Numpy (https://numpy.org/), Matplotlib (https://matplotlib.org/), OpenCV (https://opencv.org/), and Imageio (https://imageio.readthedocs.io/) were also employed. Numpy is necessary for numerical operations; Matplotlib for generating graphics; OpenCV is an agnostic package for image and video manipulation in C++; and Imageio is a package that provides functions for image manipulation, similar to OpenCV, but has been shown to be faster (80%) for extracting frames from videos.

The video used was in MP4 format, and no other video formats were tested. To extract video metadata, the open-source software MediaInfo (https://mediaarea.net) was employed. The metadata required for processing includes the orientation of the drone axes (pitch, yaw, and roll), altitude, and geographical coordinates (latitude and longitude). After the algorithm implementation, these data were transformed into functions within the package and documented, with this process being performed in the Visual Studio Code software.

For image processing, it is necessary to calibrate the drone camera to correct the lens distortion effect and improve result accuracy. Calibration also generates the parameters needed to determine the linear pixel size of the image. There are various approaches to calibration (Zhang, 2023). In this study, calibration was performed using the vertical field of view (FOV), which involves capturing an object of known dimensions within the image.

To perform the calibration procedure, the 'calibration_FOV.m' routine (Carrasco, 2019), adapted for Python, was employed. Holman et al. (2017) highlight the importance of accounting for errors in the drone camera orientation, especially deviations from the nadir position, as these can introduce inaccuracies in velocity estimates. Although lens distortion is generally a concern, previous studies suggested that, in this case, it can be disregarded. Stresser et al. (2017) found that the FOV method is not highly sensitive to calibration, agreeing with our findings in this study, in which the calibration procedure showed no significant improvements in accuracy.

However, the FOV method proves efficient for calibration when using the drone in the nadir position, being suitable for maintaining image precision. Turner et al. (2012) points out that FOV calibration is sufficient for most remote sensing applications, ensuring central image accuracy when creating georeferenced mosaics. Stöcker et al. (2017) found that, under controlled conditions and at fixed altitude, the FOV method is advantageous for operational simplicity without sacrificing data quality. James and Robson (2014) support the effectiveness of the FOV in minimizing the need for complex corrections when a consistent nadir view is maintained.

Regarding drone stability, Holman et al. (2017) developed an experiment specifically to evaluate this issue. They used DJI Phantom 3, whereas our study used DJI Phantom 4, thus similar or superior flight capabilities are expected. Their findings showed that the drone demonstrated excellent stability characteristics, with a standard deviation in horizontal and vertical position of approximately 0.20 and 0.53 m. Moreover, the wind conditions in their test were approximately 11.5 m/s, being 3 m/s in our study. Although our experiment did not assess drone

stability, according to Holman's results and the wind conditions, this issue is not a concern.

The MP4 video file, metadata parameters, and calibration parameters were employed as input for data processing to generate current values. Table 1 summarizes the steps to perform the processing, as well as software and package dependencies. Frames were extracted from the video and converted to grayscale. Each frame was segmented into predefined subframes, whose size was adjusted based on the desired spatial resolution and also constrained by the wavelengths of the captured waves (Stresser et al., 2017). These subframes were used to generate velocity vectors, and the size adjustment depends on the wave number being measured. Increasing this area enables the inclusion of a larger number of waves in the dispersion relation analysis, enhancing the robustness of the fit. However, larger areas reduce spatial resolution, which decreases the number of measurements per square meter. Therefore, it is necessary to strike a balance between robustness and resolution to optimize results.

Additionally, the adjustment depends on the analyzed wave field, with predefined parameters being input into the algorithm. The overlap between subframes can also be adjusted, considering that greater overlap results in a higher number of measurements, which in turn improves the resolution of the processed data.

The process to generate currents was conducted for each subframe separately, and the transformation of pixel intensity image to wave number was performed via the Fast Fourier Transform (FFT).

Table 1. Sequence of package processing steps and their software, language, or library requirements.

Step	Process	Dependencies
1	Load video (MP4)	Python/OpenCV
2	Get Metadata Latitude, longitude, pitch, roll, altitude	MediaInfo
3	Calibration file	Python
4	Video processing 1 – Extract frames (imageio/openCV) 2 – Convert to grayscale (imageio/openCV) 3 – Pixel to meter conversion (np) 4 – Split image into sub-frames 5 – Sets parameter limits 6 – 3D FFT 7 – Adjustment of the dispersion equation 8 – Georeferencing x, y, u, v	Python/OpenCV/Numpy/Imageio
5	Graphical presentation	Python/Matplotlib

The FFT is performed in 3D, being two-dimensional for the spatial coordinates of each frame (each row and each column), and the third dimension being for the time of the video period used for processing (for each pixel). The results of the FFT provides the wave number (K) for spatial series, and the radial frequency (ω) for temporal series (Supplementary Material Figure S1). The limits of K and ω are established and can be modulated according to the study environment.

By utilizing the wave dispersion relationship, it becomes possible to separate the spectral energy related to surface waves from noise, obtaining the current vector (U) which presents components (u and v).

$$\omega = \sqrt{g|k|tanh(|k|h)} + K \cdot U \quad (1)$$

In which ω is the radial frequency (rad/s), g is the acceleration due to gravity (m/s²), k is the wave number (rad/m), h is the water depth, and U is the current vector with components u and v.

The values of currents u and v are generated based on the best fit within the specified limits to maximize the signal-to-noise ratio (SNR), which uses the pre-defined limits of currents that may

be acting in the environment. The process of obtaining SNR is conducted in two steps, in which the energy is divided by the number of spectral bins belonging to the waves and noise, respectively, then associating both levels of energy density (Equation 2). First, the SNR is estimated using all possible values within the limits with an accuracy of 0.1 m/s, with the results obtained from the first adjustment, a second attempt is performed on the new values of u and v, thus generating results with greater precision (0.001 m/s).

$$SNR\,(u,\,v) = \frac{\sum P\,(Kx,\,Ky,\omega)_w n_n}{\sum P\,(Kx,\,Ky,\omega)_n n_w} \qquad (2)$$

In which n_w is the number of spectral bins to waves and n_n is the number of spectral bins to noise, and u and v, each one with a maximum and minimum value corresponding to the limits of the current range that can be observed in the environment (Stresser et al., 2017).

The final result is a georeferenced vector field with resolution matching the size of the subframes specified in the processing. The presence of elements such as land, boats, etc., in the images produces spurious data. The removal of these data is performed via a mask indicating the boundaries of the land.

During the process of adapting the code provided by Carrasco (2019), it was necessary to understand the algorithm and potential differences that could exist in the operation between Matlab and Python. The code was initially worked on in the Jupyter Lab IDE, being modified, refined, and tested for efficiency and agreement with Matlab. Comparisons were conducted using the same input parameters and verifying the agreement between the results via correlation and coefficient of determination (r^2), as well as root mean square error (RMSE) (Equation 3).

$$RMSE = \sqrt{\frac{1}{n}\sum (Python - Matlab)^2} \qquad (3)$$

Once the comparison between Python and Matlab results proved nearly identical, the processing functions were organized into a package called PyDroneCurrents, and a tutorial for application was developed and made available on GitHub (https://github.com/flavia-macedo/PyDroneCurrents).

Study Area

We conducted an initial assessment of the technique for obtaining currents from drone-captured videos in an area with a relatively homogeneous current field (Macedo et al., 2023). In the present case, the objective was to evaluate its effectiveness considering the flow in an area with complex morphology, where greater variations in velocity and current direction are expected. The chosen test area is the Saco da Mangueira embayment, in the estuary of Lagoa dos Patos (Figure 1).

Saco da Mangueira is a shallow cove covering approximately 23 km², roughly rectangular with dimensions of 10 × 2.5 km, and an average depth of < 3 m. Its current connection to the estuary of Lagoa dos Patos shows a width of 200 m, having been straightened by engineering works and currently forming a bottleneck between the cove and the estuary (Monteiro et al., 2005). Its shores are occupied by urban areas of the city of Rio Grande (north shore) and by an organic fertilizer industrial park (south shore) (Baumgarten et al., 2001). The hydrodynamics are associated with those of the estuary, primarily conditioned by wind patterns that control exchanges between the lagoon and the ocean (Hartmann and Schettini, 1991; Moller et al., 1996; Fernandes et al., 2002, Santa-Rosa and Schettini, 2024). However, with low-intensity winds, it has been demonstrated to be strongly linked to the local wind effect (Monteiro et al., 2005). Hydrodynamic studies in this region are still scarce, underscoring the importance of further research.

This area has been previously studied (Silva and Calliari, 2022); however, no information at the appropriate scale for at the mouth. Therefore, a bathymetric survey was necessary to provide underwater morphology and allow to plan the location of current recording instruments. A bathymetry survey was conducted using a Lawrence brand echosounder model HDS Gen2, operating at frequencies of 50 and 200 Hz with data recorded internally. The echosounder data is in the proprietary 'SL2' format from Lawrence. These files were loaded into the Jupyter IDE for data processing using the Python package SLLib (https://pypi.org/project/sllib/ and https://github.com/opensounder/python-sllib).

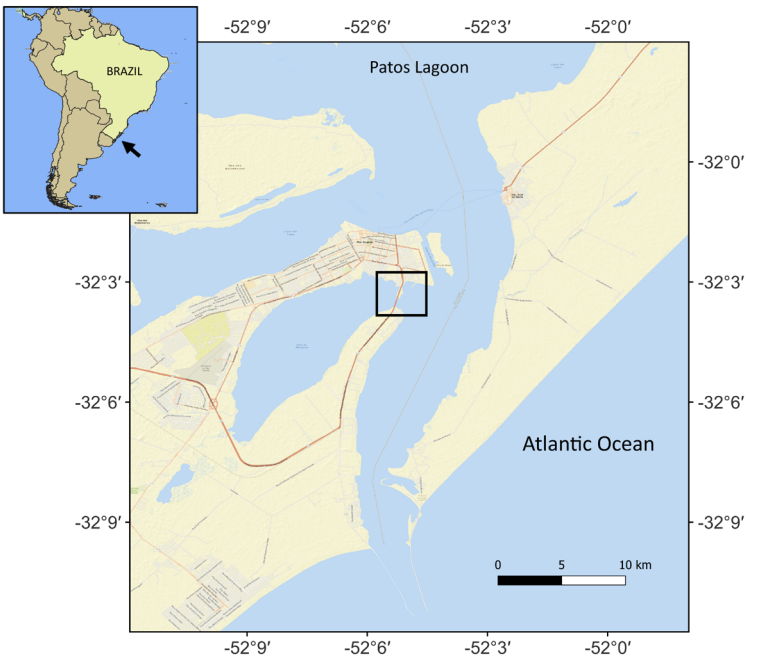

Figure 1. Location of the study area in the Lagoa dos Patos estuary, Brazil.

Field Experiment

A field campaign was conducted on June 7th, 2023, with the aim of obtaining drone videos simultaneously with direct current observations. For video acquisition, a DJI Phantom 4 Pro V2 drone was used (https://www.dji.com/phantom-4). This drone features a three-axis stabilization gimbal (yaw, pitch, and roll), and its camera records videos with resolutions from 3840x2160 toto 60 frames per second (DJI, 2023).

Current measurements were conducted using Acoustic Doppler Current Profilers (ADCP) and dye tracers. Two anchored upward-looking moored ADCPs and one vessel mounted downward-looking ADCP were used. The anchored ADCPs were Nortek Aquadopp Profiler models operating at 1000 kHz, configured to continuously record data (interval = 1 s), with a vertical resolution of 0.5 m. These ADCPs also recorded pressure to provide water level variations during the experiment. The installation positions of the ADCPs (Figure 2) were chosen based on bathymetry to align with the thalweg of the cross-section and to be within the drone line of sight according to flight planning. The position of the instruments was marked with a surface buoy used as a reference for the drone line of sight and to assist in operations with the mobile ADCP and tracer deployment. The data were reduced to average velocity every two minutes, utilizing the cell representing currents closest to the surface.

The mobile ADCP was a Teledyne RDI Workhorse model operating at 1200 kHz with bottom track. The ADCP was configured to record current profiles at 2 Hz, with a vertical resolution of 0.25 m and a blank distance of 0.4 m. Accounting for sensor depth (0.2 m), the first measurement cell was positioned approximately 0.85 m below the surface. The ADCP was mounted on a bodyboard and towed alongside the boat. Navigation involved traversing cross-sections along the main axis (Figure 2). The ADCP was operated by a computer on board the vessel using the proprietary WinRiver 2 software (RDI/Teledyne). We used a small open aluminum boat (5.5 × 1.2 m) with an outboard motor. Navigation was assisted by a Garmin portable GPS receiver (GPSmap 64), using the fixed ADCP buoys as reference points.

The drone flight planning was initially determined by altitude and the resulting imaging area. A georeferenced image generated in QGIS (https://www.qgis.org) served as the

basis and was loaded into Jupyter using the 'rasterio' package. A function was created to draw rectangles with defined sides based on the metric size of pixels, centered at geographical coordinates, and with the desired orientation. The dimensions of the rectangles correspond to the size of the camera grid at each altitude. To obtain this size in meters is necessary to know the pixel size, what depends on the altitude and camera calibration parameters. The proportions of the area at 100 meters are 140 ×80 meters high; at 200 meters, 280 × 159 meters; and at 300 meters, 420 × 236 meters. With this tool, it was possible to establish geographical coordinates where the drone would remain stationary to record videos, maximizing coverage area with local geomorphology and mosaic composition. For an altitude of 100 meters, six imaging areas were established, three on each side of the bridge, oriented at ~18° North. For altitudes of 200 and 300 meters, two imaging areas were established with an orientation of ~108° North (Figure 3).

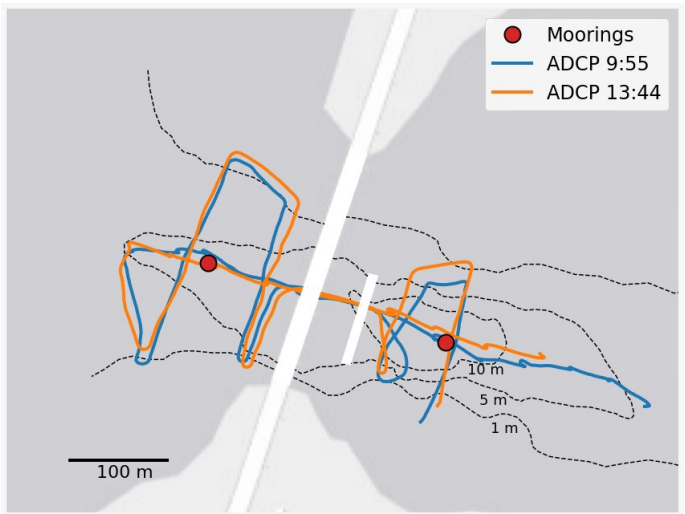

Figure 2. Indication of the anchoring locations of the ADCPs (red circles) and the navigation routes conducted for surveys with mobile ADCP. Dashed lines indicate bathymetry.

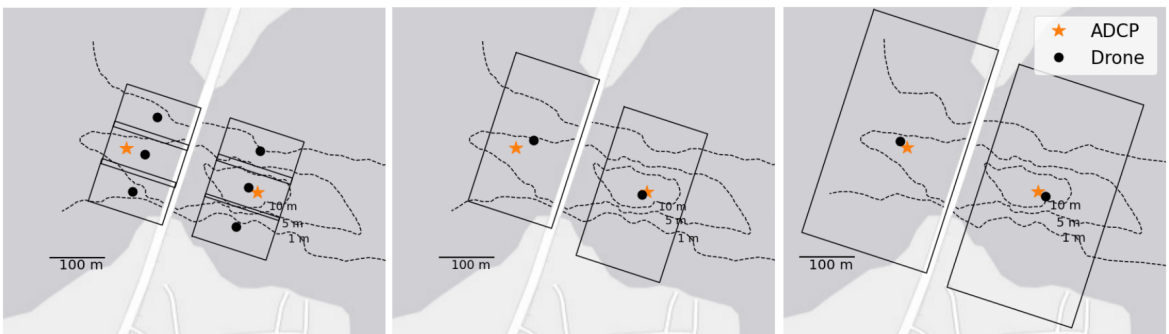

Figure 3. Planning for aerial video surveys for video recordings at altitudes of (a) 100 m, (b) 200 m, and (c) 300 m altitude.

The drone flight software did not allow pre-established flights, so the Litchi software (https://flylitchi.com) was utilized for this purpose. Although a commercial software, it comes at a low cost (~US $25.00). This software enables the planning of an automatic flight by establishing waypoints with specific parameters, including altitude, yaw, pitch, roll, and video recording time. Supplementary Material Figure S2 provides a snapshot of the planning process using Litchi for this study. For each waypoint, a 30-second video was planned with a camera tilt angle of 90°

in the vertical (nadir) direction. The videos were recorded in the resolutions of 3840 × 2160 and 2720 × 1530, with a frame rate of 24 frames per second (fps).

Some technical difficulties were encountered during the operation. Despite pre-testing the procedure to validate the operation, the drone successfully executed the planned flight at 100 meters during the field test. However, the flights at 200 meters and 300 meters experienced execution failures. The drone performed the first and last waypoints but ignored the intermediate ones. Unfortunately, it was not possible to resolve this issue in the field, suggesting that an alternative application may be needed to successfully conduct this drone operation.

During the field experiment, video recordings were conducted at three different times. In the first set of recordings, flights were performed at all three altitudes. In the second set, videos were obtained at 100 and 200 meters of altitude, but it was not possible to capture videos at 300 meters due to low clouds. In the third set, videos were recorded only at 100 meters, but with a 2048 × 1080 resolution, aimed at assessing the method sensitivity to image resolution.

The videos were processed using the Python package PyDroneCurrents. Considering the scale of the workspace, each image generated by the drone was divided into 50 square subframes with sides measuring 15, 30, and 45 meters, which represent the resolutions of the current field. The pixel size in meters for altitudes of 100, 200, and 300 meters were 0.04, 0.08, and 0.11 meters, respectively.

Drone videos were also captured simultaneously with the release of colored tracer dye. This activity was conducted via coordination relying on local references (such as the bridge and buoys) and communication between the drone operator and onboard personnel. Once the drone was positioned correctly, the dye was released, and video recording commenced. As the dye moved, exiting the imaging area, the drone was repositioned to continue recording. Sodium Fluorescein dye, with a green hue, was used for its high contrast in images (Figure 4). In total, three dye releases were conducted during the experiment.

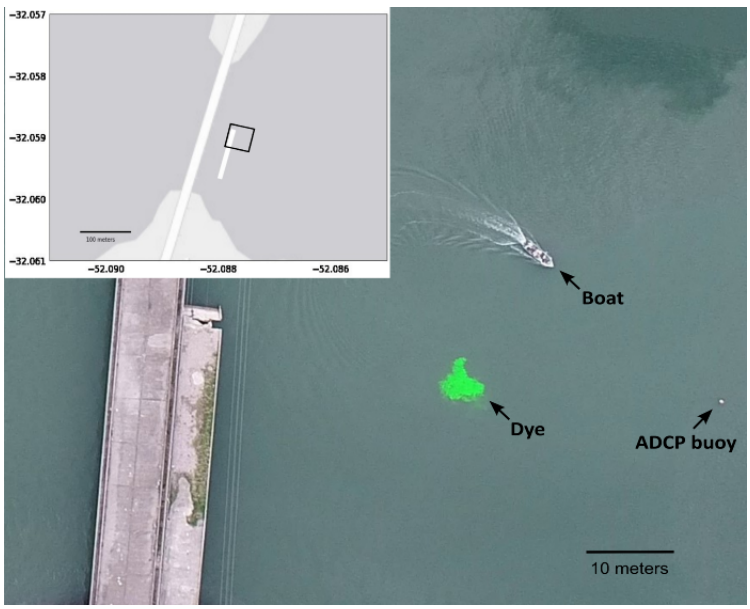

Figure 4. Moment of launching the colored tracer.

Current vectors were generated using the colored tracer method by tracking the dye displacement every 10 seconds over a total of one minute, resulting in five velocity measurements. The average of these velocities was computed for comparison (see Table 2). Frames from the dye tracking videos were extracted and georeferenced. An initial frame, captured shortly after dye release,

was chosen. From this frame, the dye perimeter was digitized to estimate its center of gravity. The same process was repeated for a final frame. The choice of the final frame was based on dye displacement and dispersion, which become more pronounced over time, causing excessive deformation. The time between the initial and final frames was determined by the number of frames, considering the recording rate (24 fps).

For the drone-generated vectors, three vectors located closest to the dye were selected. To validate the results, images with resolutions of 3840×2160 and 2048×1080 were analyzed using this method. Figure 5 depicts the timeline of operations conducted during the experiment. Priority was given to synchronizing the flights at 100 meters altitude with the recording of data using the mobile ADCP.

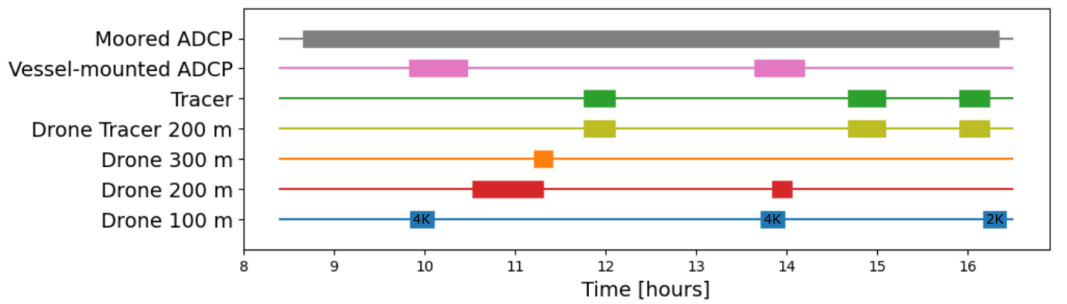

Figure 5. Indication of the anchoring locations of the ADCPs (red circles) and the navigation routes performed for surveys with mobile ADCP. Dashed lines indicate bathymetry.

The current speed values generated by the drone were compared with those recorded by the mobile ADCP, following the spatial synchronization of the data. Only the ADCP data recorded along the cross-section lines were used. The ADCP data were time-averaged over 30-second periods (60 samples), and only the first cell was considered (0.85 m below the surface). The averaged position for each interval was used as the center of a subframe for video processing. We used video footage recorded at an altitude of 100 m, with the subframe representing an area of 15 × 15 m. A total of 18 quasi-synoptic data points between the ADCP and the drone were established for each survey.

An assessment of image resolution for current field generation was also conducted. During processing, after converting frames to grayscale, they were downscaled via simple averaging by factors of 2, 3, and 4 to reduce pixel count, resulting in images of sizes 1920×1080, 1280×720, and 960×540. The subsequent processing steps followed the outlined procedure above.

RESULTS

Table 2 provides a comparison of the results from processing the same video using both Matlab and Python codes. Figure 6 shows the equivalent current fields. The processing time using Python (12 minutes) was about 4× faster than Matlab (45 minutes).

Table 2. Results obtained using the early and debugged version of the code, with r^2 and RMSE values of the vectors on the x-axis (u) and y-axis (v), and processing time of both Matlab (Early version) and Python (Debugged version).

	Early version	Debugged version
r^2 u	0.96	0.98
r^2 v	0.96	0.97
RMSE u (m/s)	0.014	0.013
RMSE v (m/s)	0.016	0.015
Processing time (minutes)	45	12

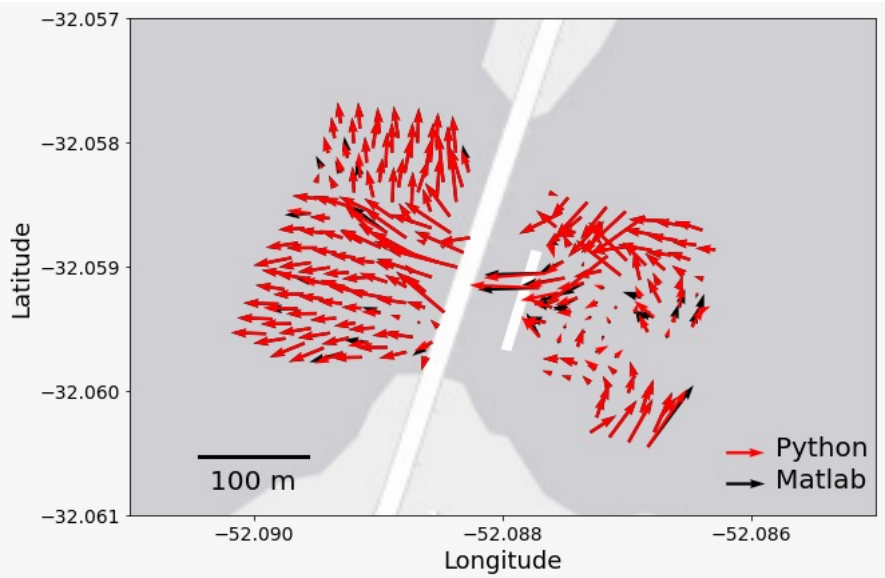

Figure 6. Comparison of a surface current field generated with Matlab (Carrasco, 2019) and Python, represented as black and red vectors, respectively.

During the field campaign day, the wind blew from the northeast at an approximately constant speed of ≈3 m/s (Figure 7a). The water level showed a slight increase throughout the day, with a variation of only 0.2 m (Figure 7b), resulting in a prevailing situation of flood currents, from the lagoon towards the inlet, for most of the time (Figure 7c). The records from the two anchored ADCPs were very similar in terms of general patterns. The maximum velocity reached 0.3 m/s, and both records exhibited high-frequency oscillations on the order of 0.05 m/s.

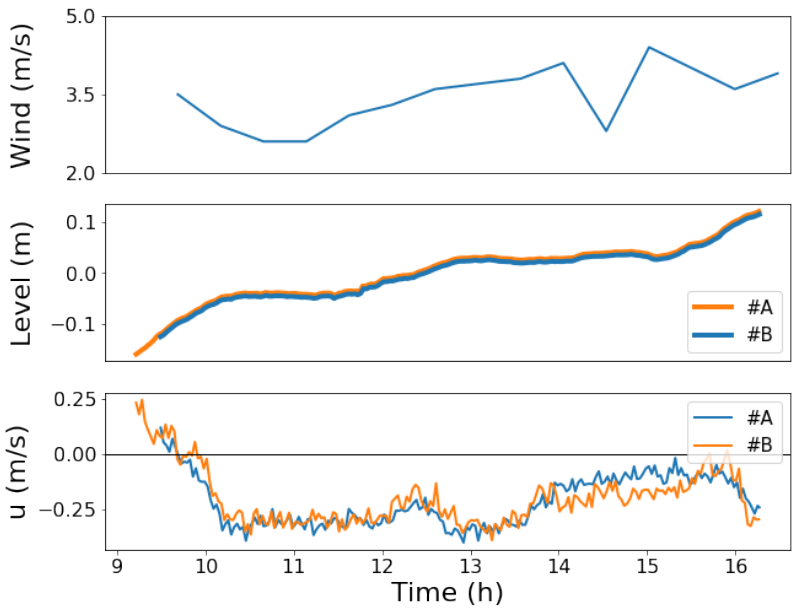

Figure 7. Time series of (a) wind speed, (b) water level variation, and (c) longitudinal current speed. #A is for bag side anchoring, and #B is for pond side anchoring.

Figure 8 shows the comparison between velocity vectors obtained from drone images at 100 meters altitude and velocities obtained with the mobile ADCP for both surveys. In both situations, the currents exhibited speeds ranging from 0.1 to 0.3 m/s. Both types of observations similarly represent the general patterns of currents, with higher speeds in the thalweg and greater velocities inside the inlet than in the lagoon. The correlation between drone and ADCP current values for the u component of velocity was better than that for the v component. Both show a direct relationship, but with a wider spread of values for the v component, which essentially represents currents transverse to the channel. The r-squared values were 0.58 and 0.11 for comparisons between the u and v components, respectively, with RMSE of 0.08 and 0.10 m/s, respectively.

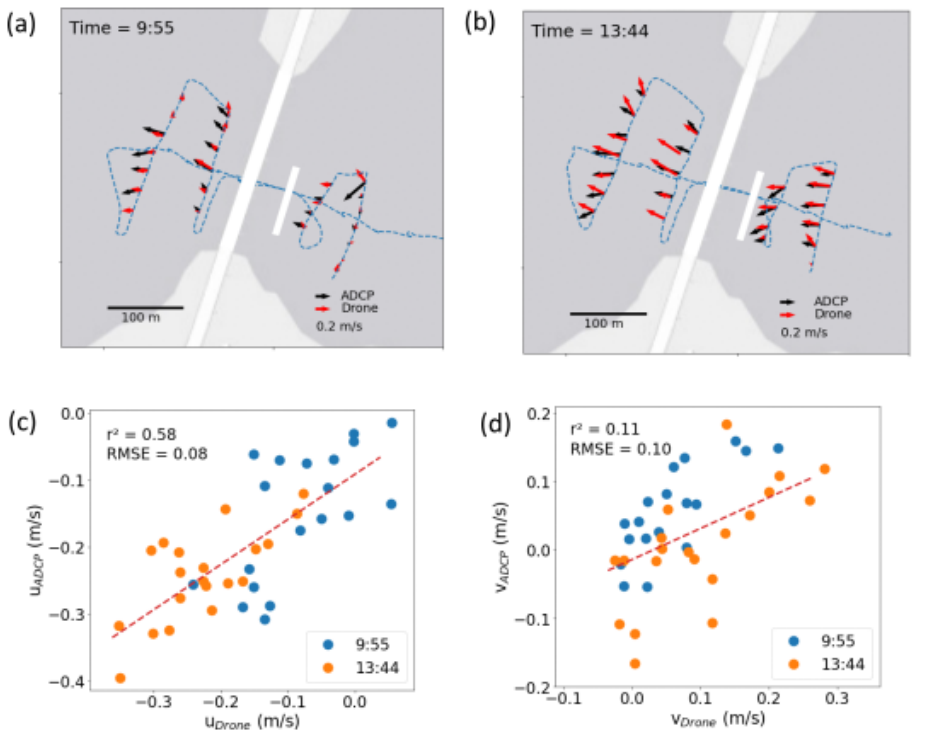

Figure 8. (a) and (b) comparison between the surface current vector fields obtained from videos recorded at 100 m altitude with the current vectors obtained with the mobile ADCP; (c) and (d) correlations between the orthogonal velocity components u and v, respectively.

Figure 9 illustrates one of the tracer dye tracking scenarios. The comparison between current vectors generated by this technique proved to be more challenging, resulting in a smaller number of sample pairs. Table 3 presents the results of current velocity obtained using the tracer dye. Comparative results between drone and tracer vectors showed a similar pattern. Table 4 shows the current velocity values generated by both methods from images at two different resolutions. The magnitude value of vectors in 3840×2160 for the tracer was 0.284 m/s with a direction of 285.3°, and for the drone, it was 0.312 m/s with a direction of 299.9°, showing a difference of 8.9% between them. However, the difference in vectors is only 1.1% for the x-axis and 51.9% for the y-axis. At 2048×1080 resolution, the vectors generated by the tracer had an average velocity of 0.319 m/s with a direction of 256.2°, being 0.342 m/s with a direction of 254.7°for the drone, corresponding to a difference of 6.7%. The difference for the u vectors was 6.1%, and for v vectors, it was 15.5%.

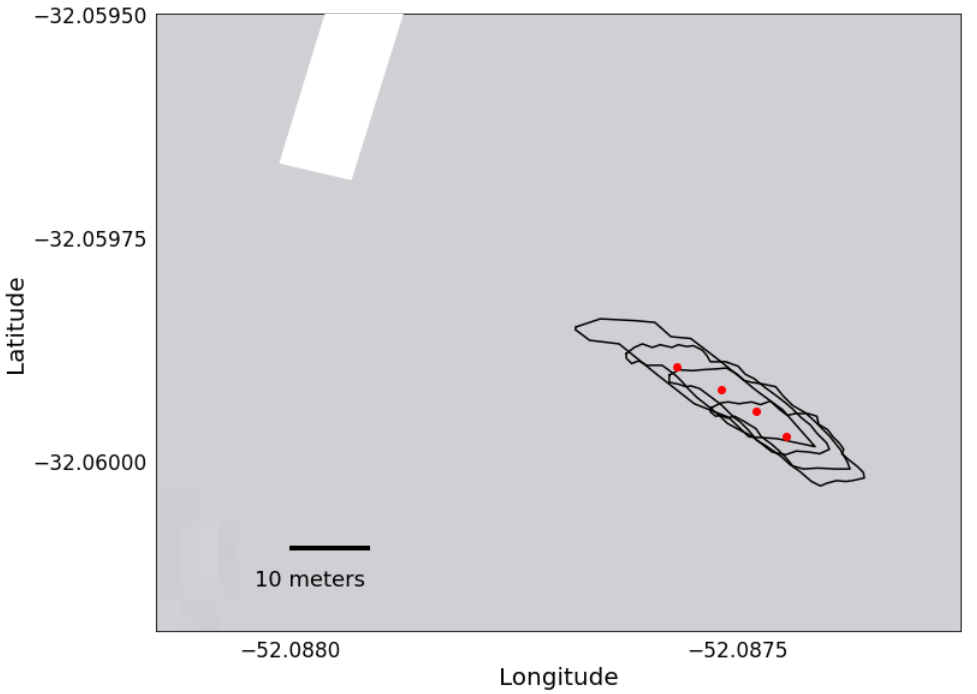

Figure 9. Representation of the stain evolution of the colored tracer at time intervals every 20 seconds, with the centers indicated by the red dots.

Table 3. Current speed results for the u and v components based on the color tracer monitoring, with videos in 3840×2160 and 2048×1080 resolution.

Time [seconds]	Resolution 3840×2160		Resolution 2048×1080	
	u (m/s)	v (m/s)	u (m/s)	v (m/s)
10	0.378	0.098	0.301	0.046
20	0.162	0.085	0.298	0.082
30	0.301	0.087	0.323	0.048
40	0.297	0.079	0.309	0.134
50	0.261	0.052	0.290	0.056
60	0.246	0.051	0.339	0.094
Mean	**0.274**	**0.075**	**0.310**	**0.076**

Table 4. Current speed results for the u and v components from videos recorded by the drone in 3840×2160 and 2048×1080 resolution.

Vectors	Resolution 3840×2160		Resolution 2048×1080	
	U [m/s]	V [m/s]	U [m/s]	V [m/s]
1	0.315	0.185	0.375	0.111
2	0.230	0.112	0.293	0.070
3	0.267	0.170	-	-
Mean	**0.271**	**0.156**	**0.33**	**0.09**

Figure 10 shows the comparison of the surface current fields generated with videos captured at altitudes of 100 and 200 m, whereas Figure 11 shows these results for altitudes of 200 and 300 m. These comparisons were possible on the western side of the bridge only due to technical issues in drone operation. Specifically, the planning executed by the Liltchi software worked well at 100 m but failed at 200 and 300 m, despite using the same parameters. The issue was identified during the operation, and it was not possible to resolve it to implement the initial plan at the time. Considering only the obtained fields, the results from speeds of 100 to 200 m agree well, but the agreement between data obtained at altitudes of 200 and 300 m is quite weak for both velocity components. This is explained by the different moments of video capture, with distinct environmental conditions (cloudiness) that may have caused reflections and deterioration of video quality at 300 m.

The approach of comparing surface current fields from videos recorded at different altitudes aims to assess the method performance in obtaining vector fields over larger areas in less time. However, this involves comparing videos recorded at various times and, consequently, under varying environmental conditions, which must be considered when analyzing the results.

To complement the above approach, the resolution of the images was reduced by 2×, 3×, 4×, and 5×via simple arithmetic averaging between pixels of the frames. Using the results generated from the degradation of image quality, the parameter r^2 was estimated, comparing each resolution with the originally used resolution (3840×2160) (Table 5).

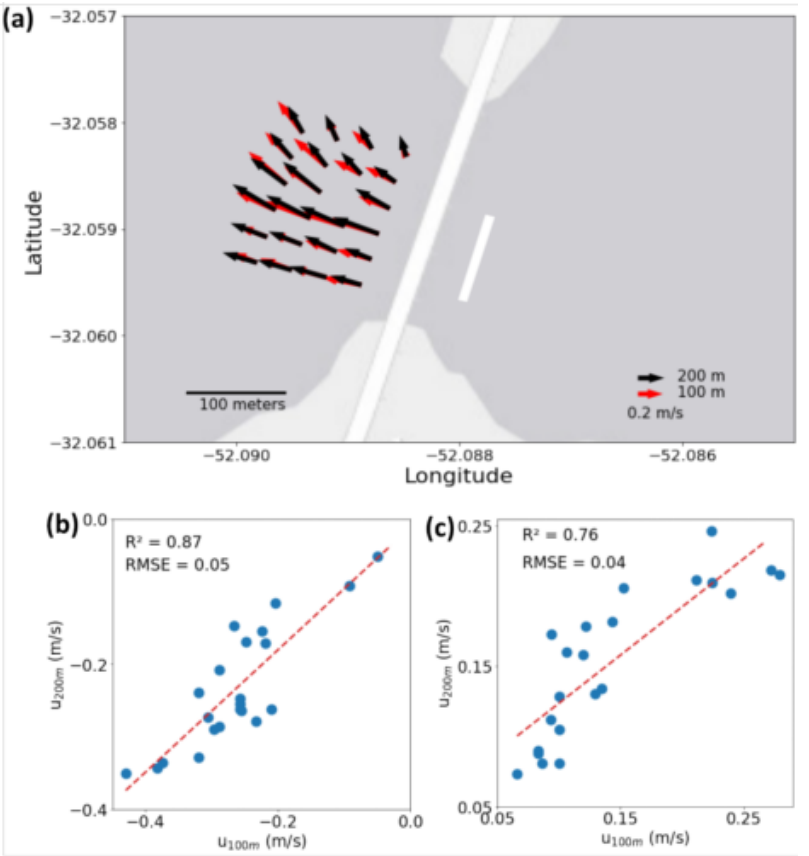

Figure 10. (a) Comparison of surface current fields generated by videos recorded at altitudes of 100 and 200 m; (b) and (c) Relationship between the u and v components.

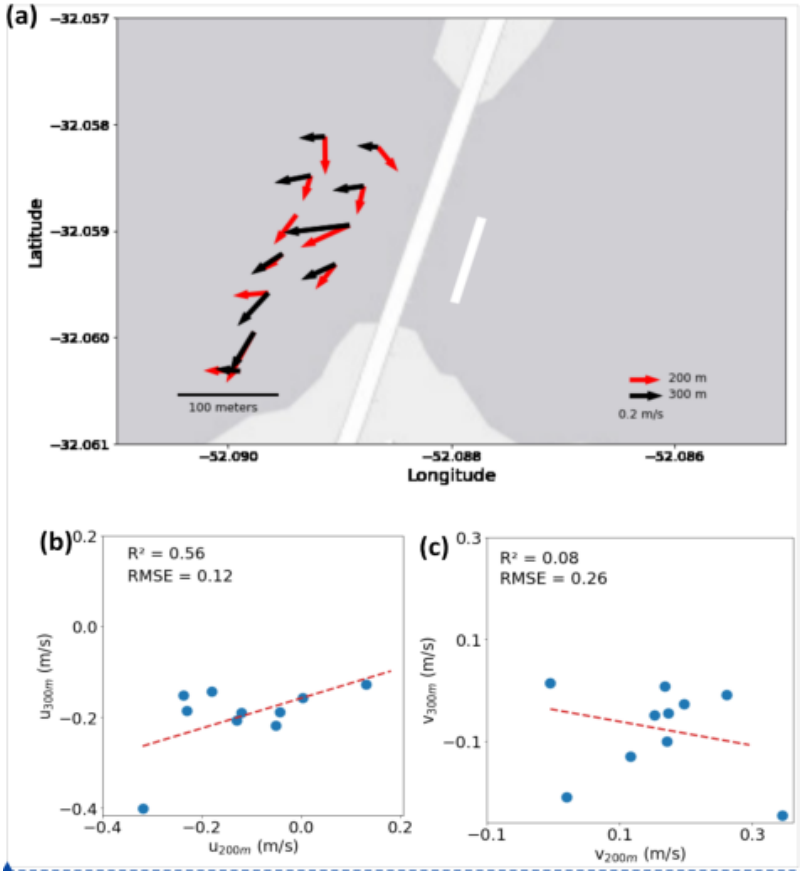

Figure 11. (a) Comparison of surface current fields generated by videos recorded at altitudes of 200 and 300 m; (b) and (c) Relationship between the u and v components.

Table 5. Processing time and comparison of results for video processing at various resolutions expressed in terms of r^2.

Frame resolution	Time processing	u r^2	v r^2
3840 × 2160	1:08:10		
2720 × 1530	0:37:00	1	1
1920 × 1080	0:17:49	0.99	0.99
1280 × 720	7:20	0.96	0.95
960 × 540	4 :36	0.88	0.93

DISCUSSION

The potential use of drones for current measurement studies via the Lagrangian approach, tracking features or objects, is an objective and proven technique. Obtaining surface current fields by applying the wave dispersion relation as presented by Stresser et al. (2017) opens up a range of possibilities for exploring observations of hydrodynamic processes that would not be possible with traditional techniques. Like any observational technique, this method shows advantages and disadvantages. For advantages, we highlight the low operational costs and improvement of drone quality every year, with costs decreasing, especially when compared to the expenses associated with traditional current measurement equipment such as ADCPs.

In addition to the cost advantage, not depending on vessels is extremely appealing for studies in environments that are difficult to access.

This is reflected in the possibility of a very rapid response time for obtaining current data, from mobilization to observation and report generation. Image collection can be completed in a short period, and data processing can be conducted within minutes once protocols are established. Thus, the technique becomes highly attractive for assessing hydrodynamic conditions in emergency situations, such as the release of toxic substances into the water.

Previous studies have already demonstrated the possibility of using drones to measure currents in river channels (Stresser et al., 2017) and estuaries (Macedo and Schettini, 2023). This study verified the methodology in a different environment than the previous ones, which shows a flow constriction through a short inlet, confirming the validation of the method even in a complex and dynamic environment. Validation was based on the use of two techniques: colored tracers and ADCPs (mobile and anchored). The use of dyes holds the advantage of being relatively simpler and can provide velocity near the surface, making it more compatible with the data generated by the drone. On the other hand, it is more challenging to obtain a larger quantity of synchronized values for comparison. The option to measure currents via ADCP provides a better possibility of controlling where the measurements will be obtained but does not enable obtaining velocity values near the surface. Due to acoustic signal interference near the surface and the level of the transducers, the closest measurement to the surface is around 1 m below.

A challenge in the comparison using the colored tracer was that in the studied environment, the vectors chosen in the drone image could not be consistently located over the area occupied by the stain. It was observed that the different water coloration due to the dye hindered the FFT ability to obtain wave parameters, as it relies on pixel intensity for this purpose. The results obtained from the comparison with tracers were not robust due to the limited number of sample pairs. However, the few pairs obtained showed good agreement.

The comparison of current results obtained from flights at 100 and 200 meters agreed well. However, the comparison between altitudes of 200 and 300 meters was poor. This is attributed more to atmospheric conditions than to the technique itself. This emphasizes a limitation of the technique, which is its dependence on atmospheric conditions for effective use. The presence of low clouds and/or strong winds limits its applicability, as well as the luminosity and angle of incidence of sunlight, which can cause reflection.

The use of drones also proved to be less sensitive to the resolution of the images generated at 100 meters altitude, with virtually no difference observed even at resolutions up to 3× lower than the original 3840×2160 resolution. This result is significant as it suggests that satisfactory results can be obtained with lower-resolution videos from inferior cameras, reducing the memory requirements for data storage. Perhaps even more relevant, the use of lower-resolution videos drastically reduces processing time. This is especially important when quick-response studies are needed. In this regard, we also emphasize that the Python code executed faster than the Matlab code. Execution speed can be further optimized with the use of parallel processing or Python supersets like Cython (https://cython.org/) or Mojo (https://www.modular.com/mojo).

The process of generating mosaics of the current field from multiple lines of sight (Figure 5) proved to be efficient in providing higher spatial resolution of the vector field for much larger areas than the field of view of each individual shot. The results were generally coherent; however, we found a consistent change in the direction of currents at the intersections of individual fields. This could be caused by distortion at the edges of the image due to the lens.

CONCLUSION

The feasibility of using drones for obtaining surface current data was assessed and validated via comparison with direct current measurements using ADCPs and colored tracers. The technique was tested for its efficiency limitations with various experiments, comparing different flight altitudes and resolutions. The use of drones for obtaining surface current fields proved to be highly effective, showing good agreement with direct

observations. It also exhibited little sensitivity to relatively low-resolution videos, significantly reducing processing time. The implementation of the technique in Python enables its use with open-source software. Future studies should test its efficiency under dffferent conditions, considering environmental variables, study regions, solar angles, and different camera calibration methods.

Data availability statement

The data that support the findings of this study are available from the corresponding author upon request.

Supplementary material

The supplementary material is presented in the Appendix.

Acknowledgments

We would like to express our gratitude to all the individuals who provided assistance during the intensive field experiment, especially to Augusto who piloted the drone.

Funding

We thank the Brazilian National Science Council (CNPq, #316037/2021-4), viaINCT-COI and PELD Estuário da Lagoa dos Patos. This study was financed by the Human Resource Program of The Brazilian National Agency for Petroleum, Natural Gas, and Biofuels – PRHANP, supported with resources from oil companies considering the contract clause nº 50/2015 of R, D&I of the ANP.

Author contributions

F.S.M.: Investigation; Methodology; Formal Analysis; Visualization; Data Curation; Writing – original draft; Writing – review & editing.

C.A.F.S.: Investigation; Methodology; Formal Analysis; Visualization; Data Curation; Writing – original draft; Writing – review & editing.

Conflicts of interest

The authors declare that they have no competing interests.

REFERENCES

Adrian, R. & Westerweel, J. 2011. *Particle Image velocimetry*. Cambridge: Cambridge Univeristy Press. 558p.

Baumgarten, M. G. Z., Niencheski, L. F. H. & Veeck, L. 2001. Nutrientes na coluna da água e na água intersticial de sedimentos de uma enseada rasa estuarina com aportes de origem antrópica (RS – Brasil). *Atlântica*, 23, 101–116.

Bowden, K. F. 1983. *Physical oceanography of coastal waters*. Southhampton: Ellis Horwood, 302p.

CARRASCO, R. 2019. CopterCurrents. Available from: GitHub. https://github.com/RubenCarrascoAlvarez/CopterCurrents. Access date: 2023 Sep. 28.

Chapman, R. D., Shay, L. K., Graber, H. C., Edson, J. B., Karachintsey A., Trump, C. L. & Ross, D. B. 1997. On the accuracy of HF radar surface current measurements: Intercomparisons with ship-based sensors. Journal of Geophysical Research, 102, 18737–18748.

Chickadel, C. C., Holman, R. A. & Frellich, M. H. 2003. An optical technique for the measurement of longshore currents. *Journal of Geophysical Research (Oceans)*, 108(C11). https://doi.org/10.1029/2003JC001774

Chickadel, C. C., Talke, S. A., Horner-Devine, A. R. & Jessup, A. T. 2011. Infrared-based measurements of velocity, turbulent kinetic energy, and dissipation at the water surface in a tidal river. *IEEE Geoscience and Remote Sensing Letters*, 8(5), 849–853.

DJI. 2023. Phantom 4 Pro V2.0 - Technical specifications. Available from: https://www.dji.com/br/support/product/phantom-4-pro-v2. Access date: 2023 Sep. 28.

Fairley, I., Williamson, B. J., Mcilvenny, J., King, N., Masters, I., Lewis, M. & Reeve, D. E. 2022. Drone-based large-scale particle image velocimetry applied to tidal stream energy resource assessment. *Renewable Energy*, 196, 839–855. DOI: https://doi.org/10.1016/j.renene.2022.07.030

Fairley, I., King, N., Mcilvenny, J., Lewis, M., Neill, S., Williamson, B. J., Masters, I. & Reeve, D. E. 2024. Intercomparison of surface velocimetry techniques for drone-based marine current characterization. *Estuarine, Coastal and Shelf Science*, 299, 108682. DOI: https://doi.org/10.1016/10.1016/j.ecss.2024.108682

Fernandes, E. H. L., Dyer, K. R., Moller, O. O. & Niencheski, L. F. H. 2002. The Patos lagoon hydrodinamics during na El Nino event (1998). *Continental Shelf Research*, 22, 1699–1713.

Fong, D. A. & Monismith, S. G. 2004. Evaluation os the Accuracy of a Ship Mounted, Bottom-Tracking ADCP in a Near-Shore Coastal Flow. Journal of Atmospheric and Oceanic Technology, 21, 1121–1128.

Halpern, B. S., Walbridge, S., Selkoe, K. A., Kappel, C. V., Micheli, F., Casey, K. S., Fox, H. E. & Heinemann, D. 2008. A global map of human impact on marine ecosystems. *Science*, 319, 948–952.

Hartmann, C. & Schettini, C. A. F. 1991. Aspectos hidrológicos na desembocadura da laguna dos Patos, RS. *Revista Brasileira de Geociências*, 21, 371–377.

Holman, R. A. & Stanley, J. 2007. The history and technical capabilities of Argus. *Coastal Engineering*, 54, 477–491.

Holman, r. A., Brodie, k. L. & Spore, n. J. 2017. Surf zone characterization using a small quadcopter:

Technical issues and procedures. *IEEE Transactions on Geoscience and Remote Sensing*, 55(4).

James, M. R. & Robson, S. 2014. Mitigating systematic error in topographic models derived from UAV and ground-based image networks. *Earth Surface Processes and Landforms*, 39(10), 1413–1420.

Koutalakis, P. & Zaimes, G. N. 2022. River flow measurements utilizing UAV-based surface velocimetry and bathymetry coupled with sonar. *Hydrology*, 9(8), 148.

Lentz, S. J. 2022. Interannual and seasonal along-shelf current variability and dynamics: seventeen years of observations from the southern New England inner shelf. *Journal of Physical Oceanography*, DOI: https://doi.org/10.1175/JPO-D-22-0064.1

Macedo, F. S., Schettini, C. A. F. & Arigony, J. 2023. Obtaining surface current field from drone imaging. *Ocean and Coastal Research*, 71, e23015. DOI: https://doi.org/10.1590/2675-2824071.22109fm

Marone, E., Schettini, C. A. F., Siegle, E., Niencheski, L. F., Madureira, L. A. S. P., Weigert, S., Pinho, M. P. & Coletto, J. L. 2020. Oceanografia operacional. In: Lana, P. C., Castello J. (Org.). Fronteiras do conhecimento em ciências do mar (pp. 54-92). Porto Alegre: Editora da FURG.

Moller, O. O., Lorenzetti, J. L., Stech, J. L. & Mata, M. M. 1996. The Patos Lagoon summertime circulation and dynamics. *Continental Shelf Research*, 16, 35-351.

Monteiro, I. O., Pearson, M. L., Moller, O. O. & Fernandes, E. H. L. 2005. Hidrodinâmica do Saco da Mangueira: Mecanismos Que Controlam as Trocas Com o Estuário da Lagoa dos Patos. *Atlântica*, 27(2), 87-101.

Mooers, C. N. K. 1976. Introduction to the physical oceanography and fluid dynamics of continental margins. In: STANLEY, D. J. & SWIFT, D. J. (Ed.) *Mar sed transp and environ manage* (pp. 7-21). New York: John Wiley and Sons.

Novi, L., Raffa, F. & Serafino, F. 2020. Comparison of Measured Surface Currents from High Frequency (HF) and X-Band Radar in a Marine Protected Coastal Area of the Ligurian Sea: Toward na Integrated Monitoring System. *Remote Sens*, 12(18), 3074. DOI: https://doi.org/10.3390/rs12183074

Palmsten, M. L., Jozarek, J. L. & Calantoni, J. 2015. Video observations of bed form morphodynamics in a meander bend. *Water Resources Research*, 51(9), 7238-7257.

Plant, W. J., Branch, R., Chatham, G., Chickadel, C. C., Hayes, K., Hayworth, B., Horner-Devine, A., Jessup, A., Fong, D. A., Fringer, O. B., Giddings, S. N., Monismith, S. & Wang, B. 2009. Remotely sensed river surface features compared with modeling and in situ measurements. *Journal of Geophysical Research (Oceans)*, 114(C11). DOI: https://doi.org/10.1029/2009JC005440

Rodríguez, E., Bourassa, M., Chelton, D., Farrar, J. T., Long, D., Perkovic-Martin, D. & Samelson, R. 2019. The winds and currents mission concept. *Frontiers in Marine Science*, 6, 438. DOI: https://doi.org/10.3389/fmars.2019.00438

Santa-Rosa, P.r.a. & Schettini, C.a.f. 2024. Daily variability of estuary-shelf exchange at the Lagoa dos Patos's mouth. *Regional Studies in Marine Science,* 77:103633, DOI: https://doi.org/10.1016/j.rsma.2024.103633

Silva, S. C. C. & Calliari, L. J. 2022. Padrões sedimentológicos e morfológicos de uma enseada numa lagoa costeira micromaré: Lagoa dos Patos, sul do Brasil. *Pesquisas em Geociências*, *49.1*, e112719-e112719. DOI: https://doi.org/10.22456/1807-9806.112719

Stöcker, C., Nex, F., Koeva, M. & Gerke, M. 2017. Quality assessment of combined IMU/GNSS data for direct georeferencing in the context of UAV-based mapping. *The International Archives of the Photogrammetry, Remote Sensing and Spatial Information Sciences*, 42, 355-361.

Stresser, M., Carrasco, R. & Horstmann, J. 2017. Video-Based Estimation of Surface Currents Using a Low-Cost Quadcopter. *Geosci and Remote Sens Lett*, 14(11), 2027-2031. DOI: https://doi.org/10.1109/LGRS.2017.2749120

Turner, D., Lucieer, A. & Watson, C. 2012. An automated technique for generating georectified mosaics from ultra-high resolution unmanned aerial vehicle (UAV) imagery, based on structure from motion (SfM) point clouds. *Remote Sensing*, 4(5), 1392-1410.

Valle-Levinson, A. 2022. Introduction to estuarine hydrodynamics. Cambridge: Cambridge University Press, 214p.

Van Rijn, L. C. 1998. *Principles of coastal morphology*. Amsterdam: Acqua Publications.

Zhang, Y. J. 2023. *Camera calibration. 3-D Computer Vision: Principles, Algorithms and Applications* (pp. 37-65). Singapore: Springer Nature Singapore.

APPENDIX

Observations of the surface current field in morphologically complex environments using drones.

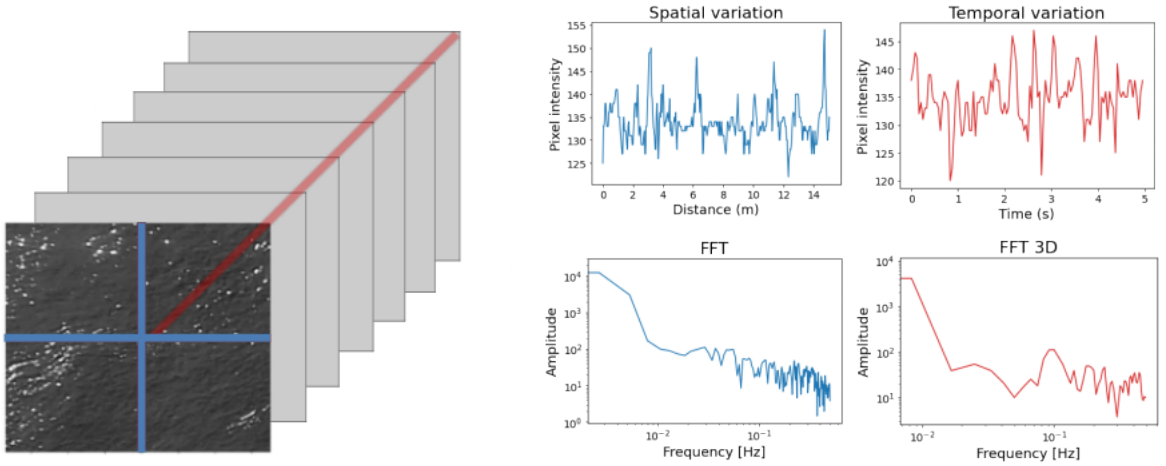

Figure S1. Representation of the 3D FFT process in the image. (a) representation of video frames showing the axes corresponding to the image size x and y in blue, and the z-axis corresponding to the number of frames in red; (b) spatial variation of the x-axis of the image showing the distance in meters on the x-axis and the variation of pixel intensity on the y-axis; (c) FFT generated from the representation in figure (a); (d) temporal variation of the video, where the x-axis indicates the time in seconds, and the y-axis indicates the variation in pixel intensity; (e) 3D FFT of the results from figure (d).

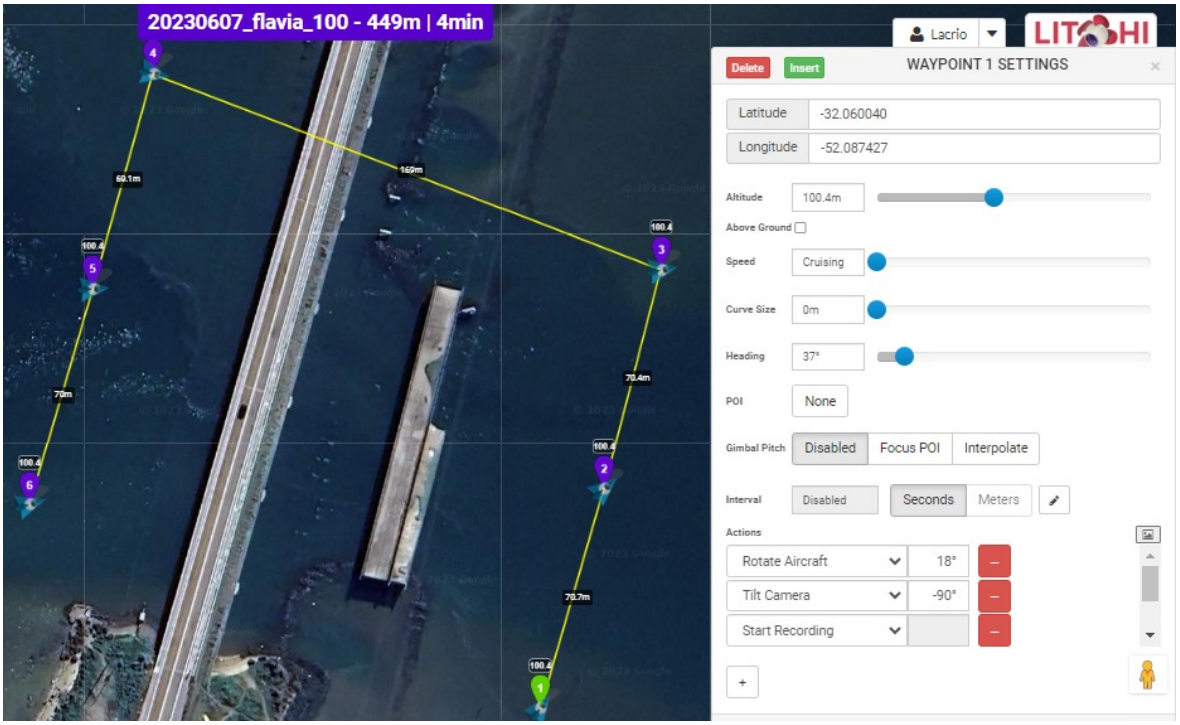

Figure S2. Liltchi software interface illustrating the area containing the flight planning at 100 meters altitude with 6 waypoints for filming. Adjacent is the box representing the configuration with flight instructions.